

# Morphology characterisation of inclusions to predict the breakdown strength in electro-ceramic materials: Microstructure modelling



Sadjad Naderi\*, James P. Heath, Julian S. Dean

Department of Materials Science and Engineering, University of Sheffield, Sheffield, UK

## ARTICLE INFO

**Keywords:**  
Electroceramics  
Microstructure  
Modelling  
Porosity

## ABSTRACT

Microstructural features such as pores, secondary phases and inclusions can significantly alter the electrical response of ceramics. Here we present a morphological finite element approach to better understand the effect of such microstructural defects on the behaviour of electroceramics. We generate irregular three-dimensional geometric models with realistic features and controllable parameters providing a method of characterising their morphology using sphericity, signifying irregularity, and projected area. The inclusion models are solved for their electrical response for changes in the material properties, making the feature either insulating or conductive in relation to the surrounding material. The electric field distribution analysis indicates the irregularity has a significant effect on the electric response, increasing the field concentration up to 12 times more than the applied field. Plotting the electric field distribution using a Weibull cumulative Probability Distribution Function we have also estimated the breakdown strength of the material. This shows that a material's breakdown strength can be reduced to 55% for an 87.5% dense sample if the inclusion is insulative and has a low sphericity or high projected area. This can be further reduced to only 40% if the feature is more conductive than the ceramic.

## 1. Introduction

Due to excellent dielectric properties and high thermal stability, granular electro-ceramics are employed in the fabrication of devices such as multilayer ceramic capacitors, positive temperature coefficient of resistance thermistors, piezoelectric sensors and transducers [1,2]. As demand for miniaturisation and performance is made from industry, control of microstructural features is crucial to maintain performance [3,4].

Microstructural features in ceramic materials range from porosity, grain boundaries to interfaces with a secondary phase and all depend on starting reagents and processing conditions during fabrication [5,6]. Previously, finite element modelling (FEM) demonstrated that porosity could lead to an increase in the local electric field [5–7]. Many of these studies have been carried out to model the role of microstructure and porosity [8,9] and reconstruct geometries which simulate the natural porous structures [10–12]. However, most use regular pore geometries (e.g. sphere) or irregular models presented in two dimensions.

Characterising the shape and morphology of such features is becoming more important in accurately simulating the structural effects on material behaviour [13,14]. Methods such as neutron, gamma ray and X-ray tomography have been utilized to provide description of the material's features [15,16]. This can, with computer-aided techniques,

be converted into a full three-dimensional microstructure in order to reconstruct the precise 3D features [17–19]. These methods require the sample to be prepared and analysed, providing not only a limited number of situations for analysis but are also time intensive.

It is known that the dielectric strength strongly depends on materials microstructures and especially on local property changes that arise from such microstructural features. These features are considered sites where polarizability is modified and charge and energy localisation can occur [20,21] and consequentially, the local concentration of the electric field can result in breakdown at an electric field much lower than the intrinsic breakdown strength of material [22]. The influence of porosity on the breakdown strength has been widely studied with previous research reporting a decrease in breakdown strength by a factor of  $\sim 3$  in dielectric materials with greater than 12% porosity [23]. An experimental and theoretical approach, used by Gerson [24] assumed that all of the pores were of equal size and uniformly distributed in the ceramic. The breakdown strength decreased abruptly, by a factor of  $\sim 2$  if the porosity reached 10%. These microstructural features generate a significant inhomogeneity of the local electric field that in turn causes a reduction in breakdown strength [25–27]. Finite element simulations have also been used to provide a statistical view of the electric field distribution. Based on a statistical analysis of local electric fields [28], it has been proposed that if a certain portion of the

\* Corresponding author.

E-mail address: [s.naderi@sheffield.ac.uk](mailto:s.naderi@sheffield.ac.uk) (S. Naderi).

<https://doi.org/10.1016/j.ceramint.2018.09.175>

Received 1 August 2018; Received in revised form 7 August 2018; Accepted 17 September 2018

Available online 18 September 2018

0272-8842/ © 2018 The Authors. Published by Elsevier Ltd. This is an open access article under the CC BY license (<http://creativecommons.org/licenses/by/4.0/>).

dielectric, determined by experiments, is under an electrical stress larger than breakdown threshold. The critical threshold value is determined by the average electric field within upper 30% of all the electric fields measured in the ceramic layer. This is obtained from a probability distribution function and the reciprocal of this value can then be linked to the breakdown strength of the material.

Accurate imitation of these features will thus improve our ability to predict the electrical behaviour. Describing the shapes are therefore key to improving analysis. Shape is the expression of an external morphology, and for some is synonymous with form. Many attempts have been made to characterise irregular shapes. Some measure the overall shape of form, whilst others concentrate more on features such as angularity versus roundness, and others on the still finer textural differences between shapes. Definitions of these can be found by Barrett [29]. One measurement technique is the sphericity of a particle which describes how closely an irregular objective resembles a sphere [30]. Using such characterisation techniques, volcanic ash particles were quantified to predict particle behaviour [31] and measured with reference to a regular shape, the most common are a circle or a sphere [32,33]. As a perfect sphere is uniquely defined by its diameter, irregularly-shaped objects need measurements of multiple dimensions [34].

In prior work, a simple sphere was used to represent the geometry of a pore but here we go beyond this simplistic approach to develop irregular microstructural characteristics. Here, we shall use the term ‘inclusion’ instead of ‘pore’ but both are synonymous, as we shall define this microstructural feature as a locally different material property inside the surrounding bulk of the grain.

We have developed a MATLAB [35] code to mimic irregular-shaped inclusions and control their shape and size independent from any existing images. To investigate how the effect of how the materials properties influence the results, two sets of simulations are made with different orders of magnitude of permittivity and conductivity, representing conductive and insulating features. The electric field distributions obtained from solving them through finite element analysis are statically analysed to achieve a comprehensive understanding of the field enhancement generated by irregular shaped features and their influence on the breakdown strength.

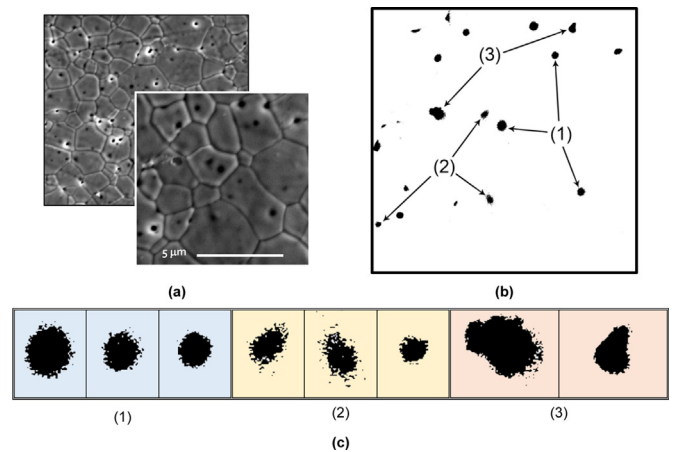
## 2. Three-dimensional geometry modelling

### 2.1. Inclusion morphology

Earlier work assumed that the inclusion was spherical, however, this is not always the case. To highlight the complexity in the microstructural features (in this case, inclusions or pores) that can be formed in ceramic materials during processing [6] we look at the SEM images of Yttria-stabilized zirconia (YSZ) processed at 1350 °C as a case study. Here we see that inter-grain porosity has various different morphologies as shown in Fig. 1a. Using image processing we can threshold and create a binary image as shown in Fig. 1b. Using the resulting image allows us to describe three main types of morphology summarising Fig. 1c. The first is a spherical type geometry, which has small deviations from being purely spherical, we shall refer to this as Cloudy. The second is a feature constructed by flatter surfaces and sharp edges which shall refer to as Voronoi. The third category is those features which contain a concave surface. Processing parameters such as the initial powder size, temperature, atmosphere and applied pressure cause these features. Furthermore, the irregular shapes emerge from the complex interaction between densification, diffusion and coarsening processes which affect the reduction in surface energy [36].

### 2.2. Computer-aided design

In this particular work, a conceptual design is proposed to mimic microstructure which is independent from tomographic images and can



**Fig. 1.** Morphological characterisation of intra-grain inclusions inspired by SEM images (a) show a typical microstructure of YSZ sintered at a temperature of 1350 °C with a zoomed in region inset. (b) For better observation, the irregular inclusions are highlighted in microstructure and (c) classified into three basic types of geometries based on their irregular attributes of (1) Cloudy, (2) Voronoi and (3) Concave.

be instrumental in FEM. A MATLAB code has been developed to construct 3D microstructures for three types of the irregular features shown in Fig. 1c which for simplicity we name these geometries as Cloudy, Voronoi and Concave. The code generates these irregular shapes inside a cube and incorporates an effective meshing technique to enhance the accuracy of numerical results (Fig. 2). The code is based on different approaches.

The code requires first a distribution of points in 3D space. These points are then passed through a combination of convex-hull [37] or Voronoi tessellation [38] algorithms. The resulting regions are then fitted with B-splines in order to reconstruct a smooth 3D microstructure that represents the typical irregular feature shown in Fig. 1c. A cube is then placed around this to replicate a grain.

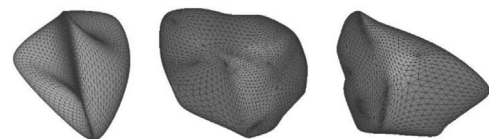
The computer-aided designs shown in Table 1 compare well with the inclusion shape in Fig. 1. A perfect sphere model is included as a comparison and to represent a regular-symmetric geometry as the reference for a comparative investigation. The reconstructed sample series are characterised with shape parameters and discussed in the next section.

### 2.3. Shape parameterisation

We parameterized the inclusions using shape parameters allowing a quantitative measure of shape for comparison. Two metrics are used, Sphericity ( $Sph$ ) and projected area ( $PA$ ).  $Sph$  is based on the ratio between the shape surface area and volume with reference to a perfect sphere as shown in Fig. 3 and is calculated using Eq. (1) [39,40]:





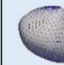



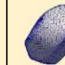



$$Sph = \frac{36\pi V_I^2}{S_I^3} \quad (1)$$

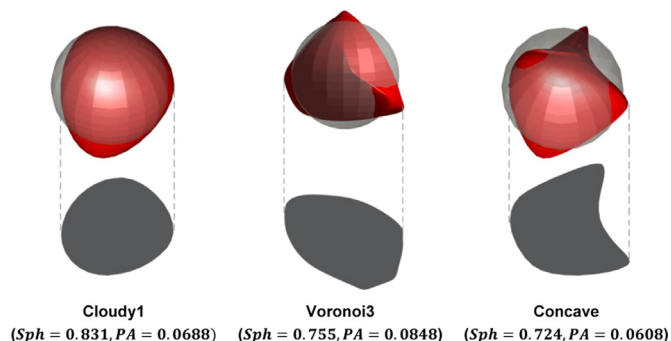
where  $V_I$  and  $S_I$  are volume and surface area of an inclusion respectively. For a perfect sphere,  $Sph = 1$ . The values of volume and surface are calculated using numerical integration methods in MATLAB. Additionally, Projected Area ( $PA$ ) here is defined as a rectilinear



**Fig. 2.** The examples of high-quality-meshed 3D models with a fine description of shape features.

**Table 1**  
Schematic of computer-aided design models and shape parameters for different irregular inclusions (note the surrounding grain is not shown) Volume is kept constant and equal to  $0.0125 \mu\text{m}^3$ .

Model Name	Sphere	Cloudy 1	Cloudy 2	Cloudy 3	Cloudy 4	Cloudy 5	Voronoi 1	Voronoi 2	Voronoi 3	Voronoi 4	Voronoi 5	Concave
Shape												
$S_f [\mu\text{m}^2]$	0.26	0.277	0.275	0.269	0.269	0.265	0.283	0.304	0.286	0.316	0.292	0.29
$PA [\mu\text{m}^2]$	0.0651	0.0688	0.0581	0.0619	0.0618	0.0595	0.0659	0.0753	0.0748	0.0879	0.0653	0.0608
$Sph$	1	0.831	0.849	0.907	0.907	0.949	0.779	0.628	0.755	0.559	0.709	0.724



**Fig. 3.** The schematics illustrate the deviation of irregular geometrical (red geometry) models from a perfect sphere (grey geometry), which is used as the reference for shape parameter measurements and the projected are of the irregular geometries are shown as the shadows (For interpretation of the references to color in this figure legend, the reader is referred to the web version of this article.).

projection on the plane perpendicular to the applied voltage.  $PA$  is effectively associated with  $Sph$  to characterize irregular geometry. The summary of shape parameters used for generating the irregular inclusions throughout this article are listed in **Table 1** where the volume is set constant for all shapes as  $0.0125 \mu\text{m}^3$  corresponding, for a perfect sphere a radius of  $0.1438 \mu\text{m}$ .

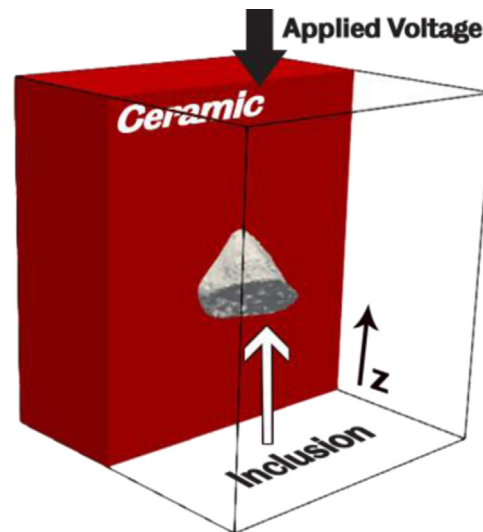
### 3. Finite element simulation

Following our previous work on spherical pores [6], we use our in-house FEM package ElCer [41] to evaluate the influence of the inclusion on the electrical response within a grain. It allows us to solve Maxwell's equations in space and time using a time domain finite element method. To study how the electrical response is altered due to the inclusion, two materials are applied, as detailed in **Table 2**. We choose two materials in order to provide a relative change of conductivity to the grain. The first is a more conductive material whilst the second is more resistive, these are also related to air and water respectively as possible materials arising from possible humidity and low density during processing.

The model starts as a solid simple solid cube of volume  $1 \mu\text{m}^3$  and resistance  $10 \text{ M}\Omega$ . This represents a fully dense grain. A potential difference is applied across the top and bottom surfaces of the grain, aligned to the  $z$ -axis generating an internal uniform electrostatic field of

**Table 2**  
Material properties used in finite element simulations for barium titanate-based ceramic and inclusions.

Material	$\epsilon_r$	$\sigma$ ( $\text{Sm}^{-1}$ )
Ceramic	1000	$10^{-4}$
Insulator (Air)	1	$0.5 \times 10^{-14}$
Conductive (Water at 20 °C)	80	$10^{-2}$



**Fig. 4.** The schematic cross-sectioned finite element model representing an inter-grain inclusion (Voronoi1) and its location inside the cube grain.

$1 \text{ MV m}^{-1}$ , this is related to the fully dense case giving the normalised electrical response  $E_N$ .

We then generate the microstructural feature in the centre the cube as shown in **Fig. 4** and solve for the electric field  $E$ , allowing for comparison between different geometry models and material properties. As the volume of the feature is set to be  $0.0125 \mu\text{m}^3$ , the corresponding density of the system is 87.5%.

### 4. Results and discussion

#### 4.1. Electrostatic field distribution

To visualise the normalised local electric field,  $E_N$  we use a combination of two approaches. As the inclusion is three-dimensional we look at two approaches to visualise the data. The first is to look at the data as a function of height ( $z$ -value) colour coding the results to indicate where the data located. The blue shaded data shows the electric field calculated less than a radius of  $0.14 \mu\text{m}$  from the centre of the system, i.e. the electric field inside the feature. This is set such that the measurement extends to just inside of the perfect sphere radius of  $0.144 \mu\text{m}$ . Red highlights the electric field around the inclusions surface between  $0.14$  and  $0.25 \mu\text{m}$  from the centre, indicating the data close to the external surface. Finally, yellow highlights the data away from the feature. In **Fig. 5** three typical models are shown for each of the model types. **Fig. 5a** show a spherical model, (b) a 'Cloudy' model and (c) a Voronoi type model. Each highlights the changes of the electric field in relation to the inclusions being assigned a resistive (air) or conductive (water) material property. The results for a Concave model are not shown here, as they produce a response very similar to the Voronoi

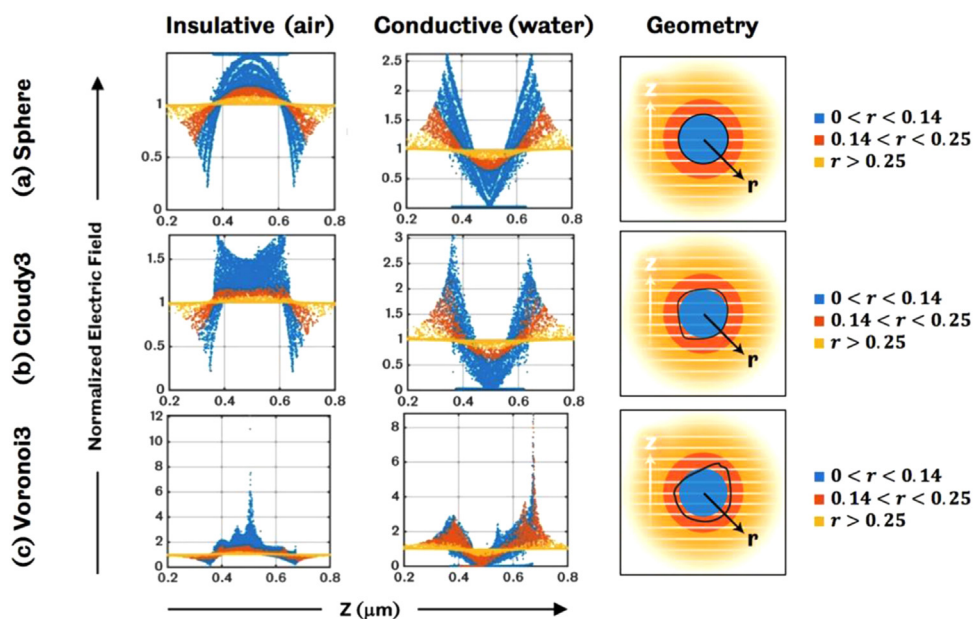


Fig. 5. The electric field profiles as a function of the  $z$  coordinate of (a) Sphere, (b) Cloudy and (c) Voronoi shaped particles. In each, the normalised electric field  $E$  is given for material properties of an insulative or conductive inclusion. The geometry highlights the colour coding. Blue is data located inside the inclusion, red near the surface and yellow highlights the electric field profile away from the inclusion, and the grey lines indicate the measured data in  $z$  (all radii are in  $\mu\text{m}$ ) (For interpretation of the references to color in this figure legend, the reader is referred to the web version of this article.).

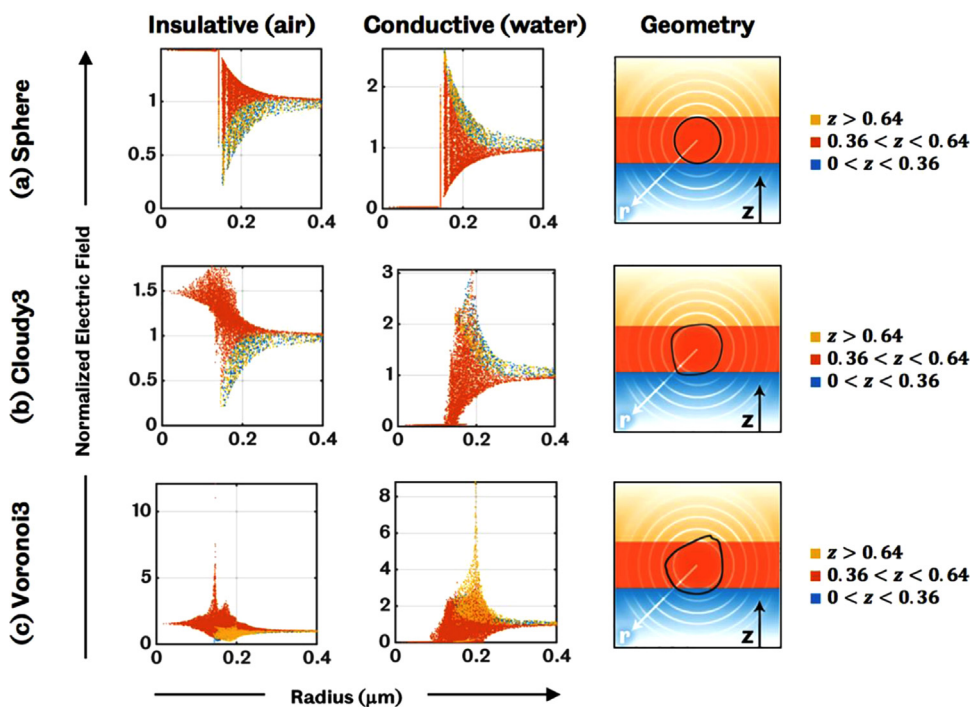


Fig. 6. The electric field profiles as a function of radial distance from the centre of the cube of (a) Sphere, (b) Cloudy and (c) Voronoi shaped particles. In each, the normalised electric field  $E$  is given for material properties of a resistive or conductive inclusion. The geometry highlights the colour coding of the distance away from the bottom surface of the inclusion with the grey spheres indicated the measured data (all lengths are in  $\mu\text{m}$ ) (For interpretation of the references to color in this figure legend, the reader is referred to the web version of this article.).

model. From this, it can be concluded that concavity does not have a distinct effect on the electric field. In all models,  $E_N$  tends to 1 away from the inclusion, indicating that the effect is confined close to inclusion.

The behaviour of the electric field around a perfect sphere inclusion ( $Sph = 1$  and  $PA = 0.0651$ ) is shown in Fig. 5a. For both types of inclusion material properties, the normalised electric tends to unity far away (yellow). If the inclusion is insulating, the electric field away from the feature starts as unity steadily dropping as it becomes close to the bottom surface of the feature. As it approaches the bottom surface (low  $z$ , blue) the electric field has fallen to only 0.2 of the initial value. As the height is increased, it quickly increases to 1.5 times (mid  $z$ , blue) and falls back to the reduced value and unity. This is converse to a conducting material where there is first a steep rise in the electric field of over 2.5 at the top and bottom of the features surface, quickly falling

around and inside the inclusion to almost zero. The symmetric response indicates that the current flows around the feature smoothly, akin to a laminar flow in fluids. It should also be noted that for a conductive inclusion the higher electric fields are experienced outside of the surface and deeper into the surrounding material, shown by the increased yellow and red data in the plot.

As we move away from a symmetric shape to that of a ‘Cloudy’ model ( $Sph = 0.95 - 0.83$ ,  $PA = 0.058 - 0.065$ ) the main electric field features are still present but the distribution starts to become asymmetrical around the inclusion, beginning to show some chaotic and turbulent features. The maximum values of electric field also are increased by approximately 10%. This highlights that the shape of the inclusion is important as the normalised electric field is very sensitive with even with small deviations from a perfect sphere. For a typical ‘Voronoi’ model ( $Sph = 0.559 - 0.779$ ) the electric field enhancement



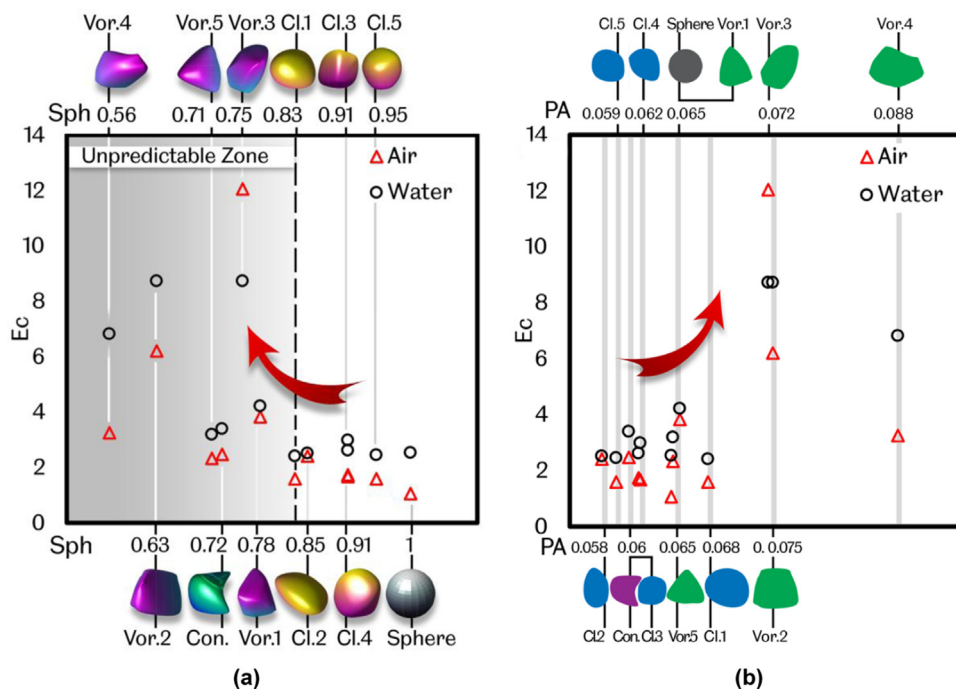


Fig. 7. The effect of sphericity  $Sph$  (a) and projected area  $PA$  (b) on the maximum electric field concentration  $E_c$  with arrows added as a guide for the eye. The grey area highlights the unpredictable zone for the maximum the electric field.

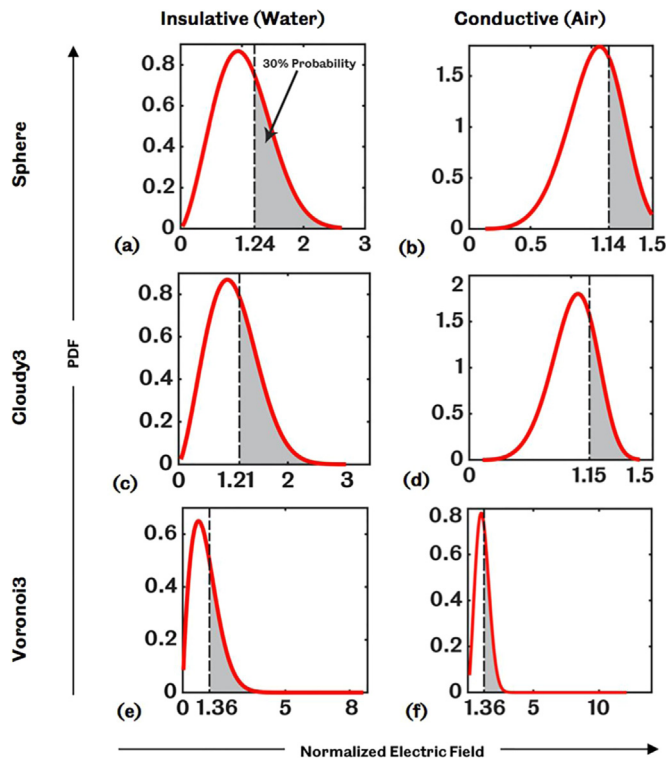


Fig. 8. Weibull cumulative Probability Density Function (PDF) of the normalised electric field influenced by the proposed intra-grain inclusion models. These are for morphologies for a sphere (a, b), cloudy (c, d) and Voronoi (e, f) structures with material properties assigned that are more insulative (air) than the surrounding material (a, c, e) or more conductive (water) shown in (b, d, f). An example is illustrated for the boundary of the upper 30% of the field on the plot of water spherical inclusion (a).

can be found to be over 8 times, three times greater than experienced for a spherical shape. If a more conductive material is used, the electric field typically increases in magnitude even further at the parts of the model, which are sharper and more pronounced, however the higher values are localised to in and around the inclusion. In general, the more irregular the feature, the electric field is more pronounced but unpredictable in comparison to the ‘Sphere’ model. This indicates a highly chaotic turbulent flow of current around the feature. If the inclusion is conductive, the higher electric fields are located around and away from the feature, whereas for an insulative region, the higher electric fields are confined and are localised inside the feature.

To also account for the model being three dimensional, we also study the electric field in the same models but this time as a function of radial distance. In Fig. 6, the normalised local electric field,  $E_N$  is plotted against the radial distance from centre of the cube. This time each region is colour coded to highlight the electric field in, near and away from the lower surface (i.e.  $z$  height). Blue shows the electric field calculated below the distance of  $0.36 \mu\text{m}$ , orange between  $0.36 \mu\text{m}$  and  $0.72 \mu\text{m}$ , and yellow above  $0.72 \mu\text{m}$ . These are related to the size of the spherical model.

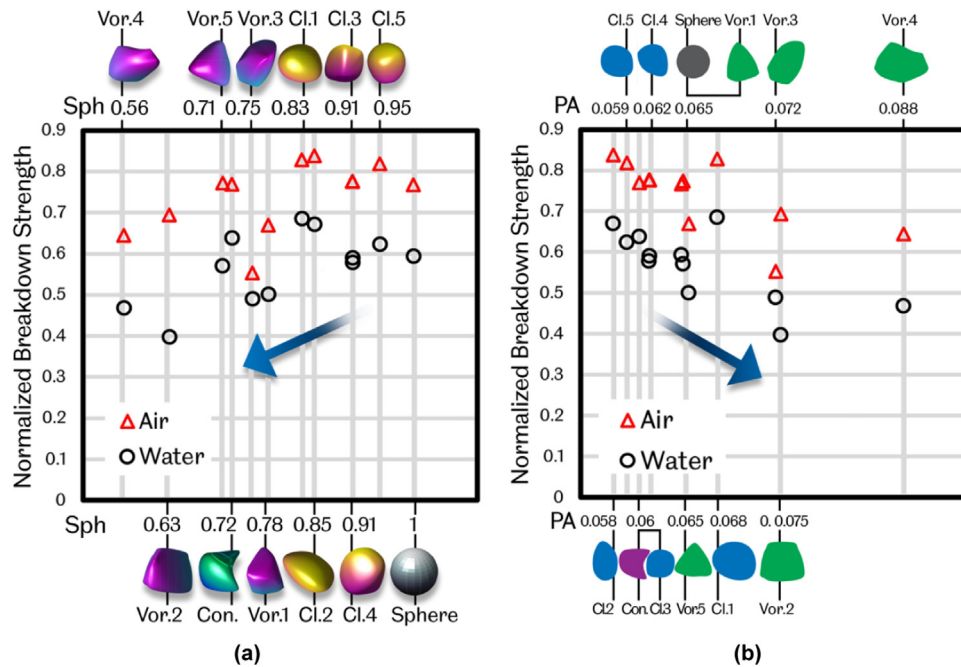
As shown in Fig. 6a, for an insulating inclusion inside the feature, the normalised electric field is already enhanced at 1.5. This falls at the models’ surface dropping again to 0.2 and back to unity, highlighting that the enhanced electric fields are localised inside the feature. For a conductive material, the electric field is first near zero inside the region and quickly rising at the surface to 2.5 times at the surface. Although this does fall, it can be seen that the enhancement of the electric field remains in the surrounding material even twice the radius of the feature.

As the shape of the inclusion is modified to ‘Cloudy’, Fig. 6b, the main features are maintained, but again, the electric field becomes asymmetrical, with also enhancements in the electric field even for insulating materials of greater than 1.5. This is further enhanced in highly irregular models to over 8 times for both types of materials, suggesting that the morphology of the feature is more significant for the maximum electric field at this point than the features material properties. The position of the field however is different with an insulating

**Table 3**

The critical values of the normalised electric field at the boundary of the upper 30% ( $E_{Cr}$ ) and the associated average of electric field within this range ( $E_{ave}$ ). The normalised breakdown strength is related using  $1/E_{ave}$ .

Model Name	Sphere	Cloudy 1	Cloudy 2	Cloudy 3	Cloudy 4	Cloudy 5	Voronoi 1	Voronoi 2	Voronoi 3	Voronoi 4	Voronoi 5	Concave	
Water	$E_{Cr}$	1.24	1.13	1.14	1.21	1.24	1.21	1.46	1.56	1.36	1.39	1.25	1.15
	$E_{ave}$	1.67	1.45	1.48	1.68	1.71	1.59	1.98	2.48	2.02	2.11	1.74	1.55
Air	$E_{Cr}$	1.14	1.06	1.07	1.15	1.13	1.08	1.27	1.24	1.36	1.25	1.12	1.08
	$E_{ave}$	1.29	1.20	1.18	1.28	1.28	1.21	1.48	1.43	1.79	1.54	1.28	1.29



**Fig. 9.** The irregularity can intensify the effect of inclusion materials and this interaction results in more field enhancement. The effect of sphericity  $Sph$  (a) and projected area  $PA$  (b) on the normalised breakdown strength obtained from the statistical analysis. The arrows are a guide for the eye.

material high values being main inside the feature (i.e. below  $0.14 \mu\text{m}$ ) whilst the conductive materials electric fields are felt by the surrounding material.

**4.2. Maximum electric field concentration**

To highlight how the different morphology of the inclusions affect the electric field concentration, we plot the maximum normalised electric field concentration  $E_C$ , found in each of the simulations, against the shape parameters for the conductive (water) and insulative (air) inclusions. This is shown in Fig. 7. The arrows are shown as a guide to the eye and indicate that features with lower  $Sph$  (more irregularity) or larger  $PA$ .

As  $Sph$  decreases from 1 (sphere) to 0.56 (Voronoi4),  $E_C$  increases irrespective of the material inside the inclusion. This is the same trend for if the projected area rises from  $0.058$  to  $0.087 \mu\text{m}^2$ . This can be related to the increased electrical field generated by geometrical factors such as large projected area, rough surfaces, asymmetric shape, sharp edges and points. If  $Sph$  is lower than 0.8 or  $PA$  greater than 0.07, an inclusion departs from the ‘shape’ of a sphere,  $E_C$  becomes unpredictable (shaded grey) due to an increase of chaotic behaviour in the way the current flows. For Voronoi3, when filled with a conductive material (air), the maximum electric field rises from 1.6 to 12; in other words, a single intra-grain inclusion can increase the electric field concentration 12 times more than for the same applied voltage across a

fully dense sample.

**4.3. Dielectric breakdown strength**

Although the maximum electric field highlights how the morphology and material property of the inclusion alter the system for irregular geometries, there exists a significant variability in the value generated. Using just the maximum value or even an average cannot fully represent properly the electric field distribution in the full system. Therefore, to achieve an effective analysis of the field distribution, a statistical approach can be used based on a Weibull cumulative function, a type of probability distribution function (PDF) shown in Fig. 8.

The Weibull cumulative Probability Distribution Function (PDF) of the normalised electric field is influenced by the different intra-grain inclusion models. Each plot in Fig. 8, shows the distribution of the electric fields in a sphere (a, b), Cloudy (c, d) and Voronoi (e, f) model for an insulative (a, c, d) or conductive (b, d, f) inclusion. For a regular shape (sphere, Cloudy) the material property provides the key features of the response. The lower the conductivity (e.g. air) the electric field inside the inclusion increases more than the regions around its surface and through the ceramic. This results in a plot with a distribution extending out to approximately 3 times the electric field with a strong peak slightly more than one as shown in Figs. 8a and 8c. Changing the material properties to a more conductive inclusion (e.g. water) alters the distribution of the electric fields. In this case, the electric field peak

still remains close to unity but as the core of the material has a near zero electric field (Fig. 5a) the distribution now extends towards zero as shown in Figs. 8b and 8d. As the microstructure alters to become more irregular, the distribution for both types of inclusions become dominated by the shape, both extending the distributions to over 8. An average or the maximum value does not describe the proportion of material that is under high electric fields as such we use a critical threshold value  $E_C$ . Here we determined this by finding the average electric field,  $E_{ave}$  in the upper 30% of all the fields experienced in the ceramic layer and summarised in Table 3 for each plot.

It can be seen that the critical threshold  $E_{Cr}$  and associated  $E_{ave}$  do not vary significantly between morphology types, however they are typically larger for the lower the sphericity or greater the projected area. A conductive inclusion (e.g. water) has on average a 30% increase in these values and as such reduces the breakdown strength further.

The reciprocal of average  $E_{ave}$  can be linked to characterise the breakdown strength of the material. This is plotted against the shape parameters and for the insulative and conductive inclusions as shown in Fig. 9. For conductive features with lower  $Sph$  (more irregularity) or larger  $PA$ , the breakdown strength can be reduced to below 40% when compared to a fully dense sample. This arises because the electric field is being enhanced around the surface of a conductive feature and away into the surrounding material, the system possesses a much higher characteristic value and as such breakdown strengths are reduced more than if the feature was more resistive.

As a comparison to previous models, we compare with the Gerson-Marshall [24] for a single pore. This model predicts the reduction in breakdown strength for an insulative material. For an 87.5% dense model with a single pore of volume  $0.125 \mu\text{m}^3$  inside a  $1 \mu\text{m}^3$  of surrounding material, the estimated reduction in breakdown strength is estimated to be 0.5. This compares well with the lowest estimate from the FEM approach using a probability distribution analysis which estimates a range of 0.84 – 0.55. However, this model does not take into account if the inclusions are more conductive than the surrounding material which, from the FEM study, can range from a 0.7 reduction in breakdown strength for a more spherical feature and even down to 0.4 for a highly irregular shape.

## 5. Conclusions

A computer-aided approach was used to replicate the irregular geometry of single intra-grain inclusion for electroceramics. The inclusions were categorized based on their shapes into three geometries of Cloudy, Voronoi and Concave. The presented models were characterised by morphology metrics such as sphericity and projected area. The intrinsic properties of the inclusion were set to mimic a resistive (air) or conductive (water) to highlight the ceramic behaviour porosity of different phases or features in the material. The electrical response distribution calculated shows enhancements of the electric field up to 12 times more than that generated by a fully dense sample. The electric field was also used to extract a critical value using a Weibull cumulative Probability Distribution Function predicting that the breakdown strength of a material falls quickly for a conductive inclusion to only 40% of a fully dense sample. Thus, to understand the reduction in breakdown strength arising from features within materials, it is not only the volume fraction or density that needs to be considered but also the morphology and material conductivity of the features.

## Acknowledgements

We thank the Engineering and Physical Sciences Research Council (EP/P019919/1) for funding and supporting this work and Ms Alison Thompson for providing the SEM images of YSZ ceramics.

## References

- [1] S. Gablenz, C. Damm, F.W. Müller, G. Israel, M. Rössel, A. Röder, H.-P. Abicht, Preparation and characterization of core-shell structured TiO<sub>2</sub>-BaCO<sub>3</sub> particles, *Solid State Sci.* 3 (2001) 291–299.
- [2] P.P. Phule, S.H. Risbud, Low-temperature synthesis and processing of electronic materials in the BaO-TiO<sub>2</sub> system, *J. Mater. Sci.* 25 (1990) 1169–1183.
- [3] S. Rout, S. Panigrahi, J. Bera, Study on electrical properties of Ni-doped SrTiO<sub>3</sub> ceramics using impedance spectroscopy, *Bull. Mater. Sci.* 28 (2005) 275–279.
- [4] F. Greuter, G. Blatter, Electrical properties of grain boundaries in polycrystalline compound semiconductors, *Semicond. Sci. Technol.* 5 (1990) 111.
- [5] M.M. Samantaryay, A. Gurav, E.C. Dickey, C.A. Randall, Electrode defects in multilayer capacitors part II: finite element analysis of local field enhancement and leakage current in three-dimensional microstructures, *J. Am. Ceram. Soc.* 95 (2012) 264–268.
- [6] G. Dale, M. Strawhorne, D.C. Sinclair, J.S. Dean, Finite element modeling on the effect of intra-granular porosity on the dielectric properties of BaTiO<sub>3</sub> MLCCs, *J. Am. Ceram. Soc.* 101 (2018) 1211–1220.
- [7] M.M. Samantaryay, A. Gurav, E.C. Dickey, C.A. Randall, Electrode defects in multilayer capacitors part I: modeling the effect of electrode roughness and porosity on electric field enhancement and leakage current, *J. Am. Ceram. Soc.* 95 (2012) 257–263.
- [8] C. Cheah, C. Chua, K. Leong, S. Chua, Development of a tissue engineering scaffold structure library for rapid prototyping. Part 1: investigation and classification, *Int. J. Adv. Manuf. Technol.* 21 (2003) 291–301.
- [9] J.K. Guest, J.H. Prévost, Optimizing multifunctional materials: design of microstructures for maximized stiffness and fluid permeability, *Int. J. Solids Struct.* 43 (2006) 7028–7047.
- [10] R. Hilfer, C. Manwart, Permeability and conductivity for reconstruction models of porous media, *Phys. Rev. E* 64 (2001) 021304.
- [11] C. Manwart, R. Hilfer, Reconstruction of random media using Monte Carlo methods, *Phys. Rev. E* 59 (1999) 5596.
- [12] C. Manwart, S. Torquato, R. Hilfer, Stochastic reconstruction of sandstones, *Phys. Rev. E* 62 (2000) 893.
- [13] K. Thornton, H.F. Poulsen, Three-dimensional materials science: an intersection of three-dimensional reconstructions and simulations, *MRS Bull.* 33 (2008) 587–595.
- [14] G. Spanos, D. Rowenhorst, A. Lewis, A. Geltmacher, Combining serial sectioning, EBSD analysis, and image-based finite element modeling, *MRS Bull.* 33 (2008) 597–602.
- [15] S. Ganti, M. Velez, B. Geier, B. Hayes, B. Turner, E. Jenkins, A comparison of porosity analysis using 2D stereology estimates and 3D serial sectioning for additively manufactured Ti6Al2Sn4Zr2Mo alloy, *Pract. Metallogr.* 54 (2017) 77–94.
- [16] L. Holzer, F. Indutnyi, P. Gasser, B. Münch, M. Wegmann, Three-dimensional analysis of porous BaTiO<sub>3</sub> ceramics using FIB nanotomography, *J. Microsc.* 216 (2004) 84–95.
- [17] M.D. Uchic, L. Holzer, B.J. Inkson, E.L. Principe, P. Munroe, Three-dimensional microstructural characterization using focused ion beam tomography, *MRS Bull.* 32 (2007) 408–416.
- [18] S. Cooper, D. Eastwood, J. Gelb, G. Damblanc, D. Brett, R. Bradley, P. Withers, P. Lee, A. Marquis, N. Brandon, Image based modelling of microstructural heterogeneity in LiFePO<sub>4</sub> electrodes for Li-ion batteries, *J. Power Sources* 247 (2014) 1033–1039.
- [19] E.M. Campo, D. Yates, B. Berson, W. Rojas, A.D. Winter, M. Ananth, J.J. Santiago-Aviles, E.M. Terentjev, Tomography of electrospun carbon nanotube polymeric blends by focus ion beam: alignment and phase separation analysis from multicontrast electron imaging, *Macromol. Mater. Eng.* (2017).
- [20] M. Touzin, D. Gœuriot, H.-J. Fitting, C. Guerret-Piecourt, D. Juvé, D. Tréheux, Relationships between dielectric breakdown resistance and charge transport in alumina materials—effects of the microstructure, *J. Eur. Ceram. Soc.* 27 (2007) 1193–1197.
- [21] A.S. Ahmed, J. Kansy, K. Zarbout, G. Moya, J. Liebault, D. Gœuriot, Microstructural origin of the dielectric breakdown strength in alumina: a study by positron lifetime spectroscopy, *J. Eur. Ceram. Soc.* 25 (2005) 2813–2816.
- [22] Y. Song, Y. Shen, H. Liu, Y. Lin, M. Li, C.-W. Nan, Improving the dielectric constants and breakdown strength of polymer composites: effects of the shape of the BaTiO<sub>3</sub> nanoinclusions, surface modification and polymer matrix, *J. Mater. Chem.* 22 (2012) 16491–16498.
- [23] E. Beauchamp, Effect of microstructure on pulse electrical strength of MgO, *J. Am. Ceram. Soc.* 54 (1971) 484–487.
- [24] R. Gerson, T.C. Marshall, Dielectric breakdown of porous ceramics, *J. Appl. Phys.* 30 (1959) 1650–1653.
- [25] P. Kim, N.M. Doss, J.P. Tillotson, P.J. Hotchkiss, M.-J. Pan, S.R. Marder, J. Li, J.P. Calame, J.W. Perry, High energy density nanocomposites based on surface-modified BaTiO<sub>3</sub> and a ferroelectric polymer, *ACS Nano* 3 (2009) 2581–2592.
- [26] J. Yao, C. Xiong, L. Dong, C. Chen, Y. Lei, L. Chen, R. Li, Q. Zhu, X. Liu, Enhancement of dielectric constant and piezoelectric coefficient of ceramic-polymer composites by interface chelation, *J. Mater. Chem.* 19 (2009) 2817–2821.
- [27] N. Frickel, A.G. Greenbaum, M. Gottlieb, A.M. Schmidt, Magnetic properties and dielectrical relaxation dynamics in CoFe<sub>2</sub>O<sub>4</sub>@PU nanocomposites, *J. Phys. Chem. C* 115 (2011) 10946–10954.
- [28] Z. Wang, J.K. Nelson, H. Hillborg, S. Zhao, L.S. Schadler, Dielectric constant and breakdown strength of polymer composites with high aspect ratio fillers studied by finite element models, *Compos. Sci. Technol.* 76 (2013) 29–36.
- [29] P. Barrett, The shape of rock particles, a critical review, *Sedimentology* 27 (1980)

- 291–303.
- [30] Y. Hayakawa, T. Oguchi, Evaluation of gravel sphericity and roundness based on surface-area measurement with a laser scanner, *Comput. Geosci.* 31 (2005) 735–741.
- [31] E. Liu, K. Cashman, A. Rust, Optimising shape analysis to quantify volcanic ash morphology, *GeoResJ* 8 (2015) 14–30.
- [32] T. Miwa, T. Shimano, T. Nishimura, Characterization of the luminance and shape of ash particles at Sakurajima volcano, Japan, using CCD camera images, *Bull. Volcanol.* 77 (2015) 5.
- [33] C.M. Riley, W.I. Rose, G.J. Bluth, Quantitative shape measurements of distal volcanic ash, *J. Geophys. Res.: Solid Earth* 108 (2003).
- [34] S.J. Blott, K. Pye, Particle shape: a review and new methods of characterization and classification, *Sedimentology* 55 (2008) 31–63.
- [35] MATLAB, The MathWorks, Inc., Natick, Massachusetts, United States.
- [36] M.N. Rahaman, *Ceramic Processing and Sintering*, CRC press, 2003.
- [37] C.B. Barber, D.P. Dobkin, H. Huhdanpaa, The quickhull algorithm for convex hulls, *ACM Trans. Math. Softw. (TOMS)* 22 (1996) 469–483.
- [38] Q. Du, V. Faber, M. Gunzburger, Centroidal Voronoi tessellations: applications and algorithms, *SIAM Rev.* 41 (1999) 637–676.
- [39] F. Alfano, C. Bonadonna, P. Delmelle, L. Costantini, Insights on tephra settling velocity from morphological observations, *J. Volcanol. Geotherm. Res.* 208 (2011) 86–98.
- [40] G. Bagheri, C. Bonadonna, I. Manzella, P. Vonlanthen, On the characterization of size and shape of irregular particles, *Powder Technol.* 270 (2015) 141–153.
- [41] J.S. Dean, J.H. Harding, D.C. Sinclair, Simulation of impedance spectra for a full three-dimensional ceramic microstructure using a finite element model, *J. Am. Ceram. Soc.* 97 (2014) 885–891.